Coexistence of ribbon and helical fibrils originating from hIAPP$_{20–29}$ revealed by quantitative nanomechanical atomic force microscopy

Shuai Zhang[a,b,c], Maria Andreasen[a,d,e], Jakob T. Nielsen[a,d,f], Lei Liu[a,b,c], Erik H. Nielsen[a,d,f], Jie Song[a,b,c], Gang Ji[g], Fei Sun[g], Troels Skrydstrup[a,d,f], Flemming Besenbacher[a,b,c], Niels C. Nielsen[a,d,f], Daniel E. Otzen[a,d,e], and Mingdong Dong[a,b,c,1]

[a]Interdisciplinary Nanoscience Center (iNANO), [b]Centre for DNA Nanotechnology (CDNA), [d]Center for Insoluble Protein Structures (inSPIN), and Departments of [c]Physics and Astronomy, [e]Molecular Biology, and [f]Chemistry, Aarhus University, DK-8000 Aarhus C, Denmark; and [g]National Laboratory of Biomacromolecules, Institute of Biophysics, Chinese Academy of Sciences, Beijing 100101, China

Edited by Alan R. Fersht, Medical Research Council Laboratory of Molecular Biology, Cambridge, United Kingdom, and approved January 8, 2013 (received for review July 6, 2012)

Uncontrolled misfolding of proteins leading to the formation of amyloid deposits is associated with more than 40 types of diseases, such as neurodegenerative diseases and type-2 diabetes. These irreversible amyloid fibrils typically assemble in distinct stages. Transitions among the various intermediate stages are the subject of many studies but are not yet fully elucidated. Here, we combine high-resolution atomic force microscopy and quantitative nanomechanical mapping to determine the self-assembled structures of the decapeptide hIAPP$_{20–29}$, which is considered to be the fibrillating core fragment of the human islet amyloid polypeptide (hIAPP) involved in type-2 diabetes. We successfully follow the evolution of hIAPP$_{20–29}$ nanostructures over time, calculate the average thickening speed of small ribbon-like structures, and provide evidence of the coexistence of ribbon and helical fibrils, highlighting a key step within the self-assembly model. In addition, the mutations of individual side chains of wide-type hIAPP$_{20–29}$ shift this balance and destabilize the helical fibrils sufficiently relative to the twisted ribbons to lead to their complete elimination. We combine atomic force microscopy structures, mechanical properties, and solid-state NMR structural information to build a molecular model containing β sheets in cross-β motifs as the basis of self-assembled amyloids.

μFS | mutants | nanomechanical map | self-assembly nanostructure

Protein aggregation and amyloid deposits (1, 2) are associated with more than 40 different diseases (3) ranging from neurodegenerative diseases such as Alzheimer's disease (4) and Parkinson disease (5) to systemic amyloidosis, such as type-2 diabetes mellitus (T2D) (6). Over the last few decades, amyloid structures and amyloid assembly have been extensively studied using a variety of diffraction techniques such as X-ray scattering and electron diffraction. However, these methods only provide average structures (7). Many structures have also been resolved in great detail by solid-state NMR spectroscopy (8, 9), which mainly represents end-point structures and, unless specifically trapping intermediates, typically does not provide a clear picture of the transient structures formed during the fibrillation process. However, it is very important to resolve the dynamics of the nanostructures of amyloids at various steps during self-assembly to understand the mechanics behind amyloid initialization, formation, growth, and maturation as well as for the design of potential drugs. Atomic force microscopy (AFM) is capable of obtaining nanoscale resolution of individual molecules or supermolecular structures. This method also allows for the analysis of the self-assembly mechanism and the driving force of aggregation (10–14). Importantly, AFM, furthermore, provides the possibility to follow the dynamics to obtain a detailed picture of the amyloid assembly process (15).

In the case of T2D, amyloid deposits, composed mainly of human islet amyloid polypeptide (hIAPP), have been found in more than 90% of T2D patients (16, 17). hIAPP is a 37-amino-acid peptide hormone, and the decapeptide SNNFGAILSS comprising hIAPP$_{20–29}$, considered to be the core fibrillating element of hIAPP relating to T2D (18, 19), is critical for the fibrillation of hIAPP and shows cytotoxicity (19). The analysis of hIAPP$_{20-29}$ fibrils revealed two distinct fibril types, comprising either parallel β-strands or antiparallel β-strands (20). High-resolution solid-state NMR structures of hIAPP$_{20–29}$ fibrils have provided detailed insight into the antiparallel hetero zipper with a twist along the fibril axis (21–23). However, no uniform detailed theory of the self-assembly behavior is available (11) and, in particular, the transitions between different intermediates during fibrillation remain to be elucidated.

Here, we apply high-resolution AFM and the recently developed microsecond force spectroscopy (μFS) for quantitative nanomechanical maps (24, 25) to explore the nanostructures and nanomechanical properties of species formed during the self-assembly of the decapeptide hIAPP$_{20–29}$. By following the temporal evolution of the amyloid peptide self-assembly process, we calculate the average thickening speed of ribbon structures, which is considered a key intermediate in the ribbon-like packing scheme (26, 27). More importantly, the coexistence of initial ribbon structures and the following helical ribbon-like fibril structures has been captured, which is strong direct evidence of a structural transition from ribbons to fibrils. Furthermore, the two single-point mutations $A_{26}G$ and $I_{27}V$ shift this balance and destabilize the helical hollow fibril sufficiently relative to the ribbons to lead to their complete elimination. By combining statistical analysis of AFM morphology images with nanomechanical maps, we propose an instructive model of mature hIAPP$_{20–29}$ involving ribbons and helical fibrils and derive a model of the self-assembly nanostructures at molecular resolution incorporating data from the recent solid-state NMR structure (21).

Results

Fibrillation of hIAPP$_{20–29}$ Follows a Nucleation-Dependent Fibrillation. The kinetic profiles of hIAPP$_{20–29}$ fibrillation were investigated using thioflavin T (ThT) fluorescence (28) (Fig. 1*A*). An initial lag phase of ~1.5 h is followed by a *ca*. 1-h increase in the ThT fluorescence leading to a plateau, indicative of nucleation-

Author contributions: S.Z., M.A., D.E.O., and M.D. designed research; S.Z., M.A., J.T.N., and E.H.N. performed research; J.S., G.J., and F.S. contributed new reagents/analytic tools; S.Z., M.A., J.T.N., L.L., F.S., T.S., F.B., N.C.N., D.E.O., and M.D. analyzed data; and S.Z., M.A., J.T.N., L.L., F.B., N.C.N., D.E.O., and M.D. wrote the paper.

The authors declare no conflict of interest.

This article is a PNAS Direct Submission.

Freely available online through the PNAS open access option.

[1]To whom correspondence should be addressed. E-mail: dong@inano.au.dk.

This article contains supporting information online at www.pnas.org/lookup/suppl/doi:10.1073/pnas.1209955110/-/DCSupplemental.

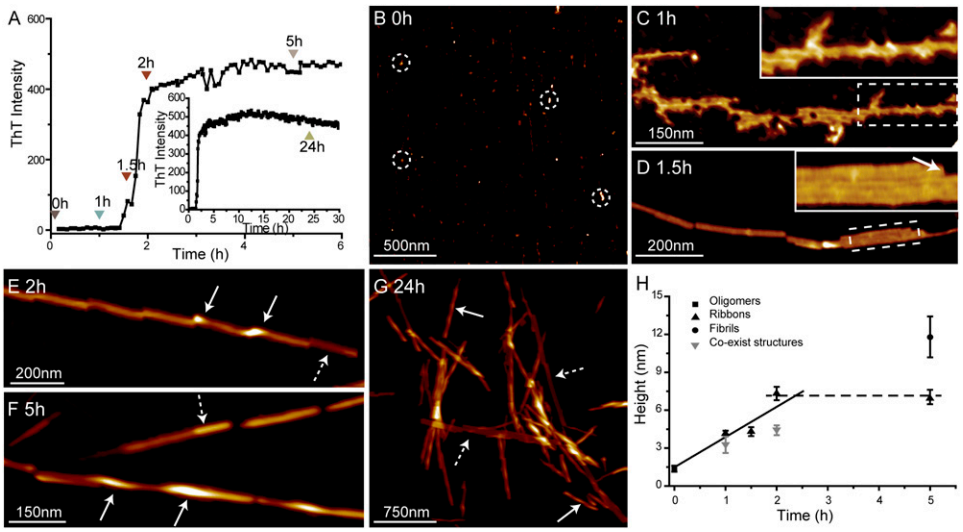

Fig. 1. ThT assay and time-lapse AFM data of $hIAPP_{20–29}$ self-assembly. (*A*) The ThT assay of the self-assembly process of $hIAPP_{20–29}$; arrows indicate the sampling times (0, 1, 1.5, 2, 5, and 24 h) for time-lapse AFM imaging. (*B*) AFM image of $hIAPP_{20–29}$ self-assembly nanostructures at 0 h; dashed circles indicate the appearance of oligomers. (*C*) AFM image of $hIAPP_{20–29}$ self-assembly nanostructures at 1 h; the high-resolution image (*Inset*) is zoomed from the dashed rectangle, which highlights the appearance of immature ribbons. (*D*) AFM image of $hIAPP_{20–29}$ self-assembly nanostructures at 1.5 h; the high-resolution image (*Inset*) is zoomed from the dashed rectangle to highlight the mature ribbon; the arrow indicates the defect of the ribbon. (*E*–*G*) AFM images of $hIAPP_{20–29}$ self-assembly nanostructures at 2, 5, and 24 h, respectively; solid arrows indicate the twisted regions and dashed arrows indicate the survived ribbons. (*H*) The heights (nm) of all $hIAPP_{20–29}$ assembly nanostructures with different incubation times (h); the fitting slop of 2.4 nm/h can be expressed as the average vertical growing speed of ribbons in the transition stage. In the plateau stage the thickness stays constant, as the dashed line indicates.

dependent fibrillation (29, 30). Circular dichroism (CD) spectroscopy and FTIR spectroscopy analysis confirm that the monomer, which displays random coil structure in the CD spectra and β-turn structure in the FTIR spectra, is transformed into a β-sheet enriched structure (Figs. S1 and S2). The β-turn structure seen for the monomer in the FTIR spectrum could be induced by an artifact of drying the monomeric peptide before the measurements. The peak observed for the monomer is very broad, a feature seen for random coil structures (31), making it reasonable to ascribe the FTIR spectrum of the monomer to a disordered structure. These optical techniques are efficient for probing overall fibril formation and average secondary structures and they show that the fibrillation of $hIAPP_{20–29}$ follows a nucleation-dependent fibrillation process. Scanning probe microscopy imaging techniques allow an exploration of the nanostructures of the self-assembled species.

Fibrillation of $hIAPP_{20–29}$ Proceeds Through Oligomeric Structures Assembling into Thin Ribbons That Finally Associate to Form Twisted Fibrils. To follow the evolution in the morphology of the different species, time-lapse AFM (32, 33) was conducted. This was performed by withdrawing samples at different time points during the dynamic fibrillation process for subsequent AFM imaging (arrows in Fig. 1*A*). The AFM imaging is carried out immediately to minimize possible effects of the substrate on the self-assembly process. This approach is able to provide valuable information on the development of fibrillation involving various species (33, 34).

At the initial time point of 0 h, no obvious amyloid structures are present; only small particles are observed (Fig. 1*B*, indicated by dashed circles) with a height of 1.4 ± 0.1 nm. After 1 h of incubation (still in the lag phase, Fig. 1*A*), several long, thin, undefined strands appear with many defects (Fig. 1*C*). Considering that it is still in the lag phase, they are named immature ribbons. During the elongation phase of the fibrillation (time point 1.5 h, Fig. 1*A*), ribbons become more frequent and their width increases (Fig. 1*D*). The ribbons display striations along their lengths, suggesting that the wider ribbons seen at time point 1.5 h are hierarchical structures, consisting of lateral associations of the immature ribbons found at time point 1 h. The immature ribbons (Fig. 1*C Inset*), compared with the later better-defined ribbons (Fig. 1*D Inset*), provide clear evidence of a hierarchical assembly process. In addition, the arrow in Fig. 1*D Inset* suggests a ribbon parallel growth mechanism.

After 2 h, the ribbons begin to partially twist into fibrils (Fig. 1*E*). This twisted morphology of the fibrils is consistent with what has previously been observed for fibrils of $hIAPP_{20–29}$ (21, 35). Such twisted fibrils have also been observed in other fibrillating systems (10, 12). However, if the ribbons are simply the precursors of the twisted fibrils, they should all be converted into twisted fibrils and no flat ribbons should be present at the end stage of the fibrillation process. Surprisingly, the morphology image at time point 5 h (during the plateau phase) proves that a large population of flat ribbons is still present (highlighted by the dashed arrow in Fig. 1*F*). Even after 24 h (Fig. 1*A Inset*), the appearance of the ribbons can still be easily identified by AFM (dashed arrows in Fig. 1*G*). This could indicate that the conversion of the flat ribbons into twisted fibrils is a very slow process; it is possible for them to coexist over a long period, even after 72 h of incubation (Fig. S3).

The average height of $hIAPP_{20–29}$ structures at different time points is plotted in Fig. 1*H*. Combining the height distribution at different time points (Fig. 1*H*) and the corresponding morphologies, a coherent picture emerges of the self-assembly process. The self-assembly process begins at 1 to 1.5 h and the ribbons form gradually from 1.5 to 2 h (the major part of the elongation phase in the ThT assay); not only do the ribbons begin to twist in this period, they also thicken gradually from 4.3 ± 0.2 to 7.3 ± 0.3 nm. Such a thickening process of the fibrils is much slower than the elongation process. Finally, the ribbon stops growing in the plateau stage.

Ribbons Are Hierarchical Structures Consisting of Narrower Ribbons Able to Transform to Fibrils. Having established which species are involved in the fibrillation, we analyzed the detailed structure of flat ribbons and twisted fibrils in a well-incubated sample (Fig. 2) using high-resolution AFM. A typical high-resolution AFM image (Fig. 2*A*) reveals the coexistence of two types of $hIAPP_{20–29}$ nanostructures, namely, the ribbon and the twisted fibrils. The twisted fibrils are considered to be the mature species of the amyloid self-assembly due to their structural complexity (11, 36). However, three kinds of twisted fibrils with different diameters, as indicated by the terms fibril 1, fibril 2, and fibril 3, are depicted in Fig. 2*A*. All of the twisted fibrils show the characteristic chirality, which may be due to the chirality of the initial peptides (37). By carefully analyzing the height of a mount of ribbons and fibrils (twisting crests), we summarized a height histogram (Fig. 2*B*) representing five distributions. Interestingly, the height values (the profiles of bb′, cc′, and dd′ in Fig. 2*D*) of fibrils 1, 2, and 3 (Fig. 2*A*) fit into three of the height distributions in Fig. 2*B*. The thickness of the ribbons is 7.4 ± 0.6 nm; that of the first fibril

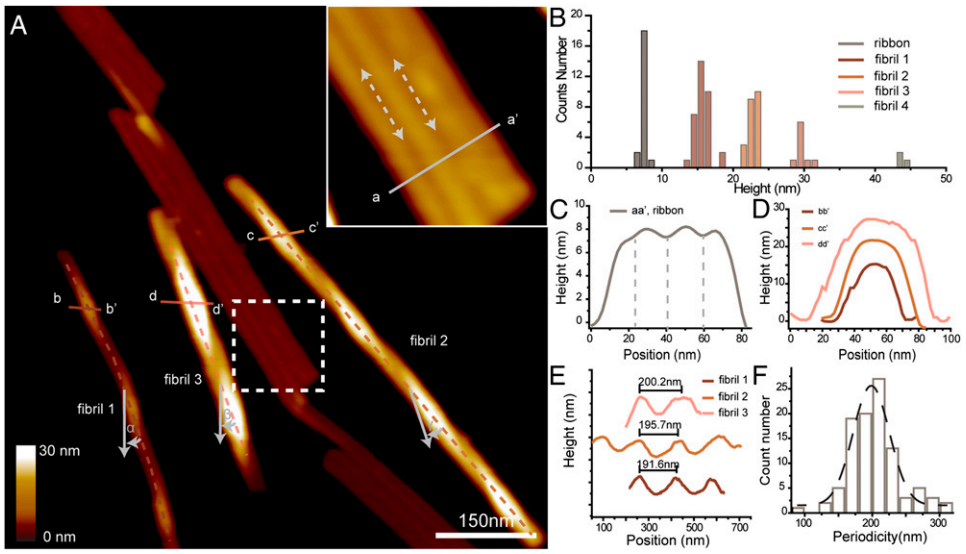

Fig. 2. Statistical analyses of hIAPP $_{20–29}$ nanostructures with high-resolution AFM. (*A*) High-resolution AFM morphology image of hIAPP$_{20–29}$ after more than 24 h of incubation; σ, β, and γ represent the angle between fibril elongation and fibril twisting direction. The inset image is zoomed from the dashed square; the gray dashed arrows in the inset image indicate the edges between two subribbons. (*B*) Height distribution of ribbons and the twisting parts along fibrils based on 89 samples. (*C*) Line profile of the multistrand ribbons, indicated in the inset image along line aa′ in *A*. (*D*) Line profiles of fibrils 1–3 indicated by the solid lines bb′, cc′, and dd′ in *A*. (*E*) Line profiles along fibrils 1–3 represent the periodicities of fibrils according to the dashed line in *A*. (*F*) Periodicity distribution of fibrils is 203.8 ± 16.8nm (SD).

distribution is 15.5 ± 0.4 nm and that of the second and third fibril distributions is 22.9 ± 0.3 nm and 29.7 ± 0.5 nm, respectively. The height distributions of the various twisted fibrils are approximately two, three, and four times the thickness of flat ribbons, respectively, which suggest that fibrils, similar to the flat ribbons, contain multiple strands.

In addition to the height, we also systematically analyzed the width of the structures. The ribbon shows clear striations along its length, indicating that it is composed of strands. The dashed arrows (Fig. 2*A Inset*) highlight that the direction of the individual strand is parallel to the long axis of the ribbon. By counting the numbers of peaks and valleys along the profile aa′ (Fig. 2*C*), four single strands can be distinguished, and the width of a single strand is ∼19.0 ± 1.0 nm. The width of the twisted fibrils in Fig. 2*A* is also measured (solid line bb′, cc′, and dd′ in Fig. 2*A*). The line profiles of fibrils 1, 2, and 3 (Fig. 2*D*) show good agreement between the height and width relationships of ribbons, being approximately two, three, and four times that of a single strand. Based on these quantitative AFM measurements, we are able to conclude that fibrils 1–3 shown in Fig. 2*A* are composed of multiple strands. This indicates that, in the bulk solution, there coexist several subpopulations of fibrils that are composed of a varying number of subribbons.

Importantly, it has previously been established that fibrils with various numbers of substrands display various periodicities (11). However, the fibrils formed in the present study all have nearly the same periodicity irrespective of the number of subribbons forming the fibril (Fig. 2*E*), as revealed from the line profile along the dashed line in Fig. 2*A*. Based on more than 200 individual measurements, the periodicity distribution of fibrils is found to be 203.8 ± 16.8 nm (Fig. 2*F*). Furthermore, all fibrils examined display the twisting angle around 21.3° (angles α, β, and γ in Fig. 2*A*).

Flat and Twisted Ribbons Display Different Mechanical Properties, Suggesting a Helical Anisotropic Fibril Structure. High-resolution AFM furthermore allows for the visualization of fibril structures to determine morphological properties in detail at the nano scale. In general, surface morphology is not sufficient to provide information underneath the detectable surface, nor does it detect the internal changes behind the differences in morphology. Hence, the information provided by the standard AFM is limited. AFM-based force-volume measurement and nanoindentation can combine sample morphology and mechanical properties, enabling the extraction of the information underlying the accessible surface morphology (38); however, its success is restricted by the poor resolution and time-consuming data acquisition. The recently developed μFS improves both the temporal speed and the resolution dramatically (39).

Two hIAPP$_{20–29}$ fibrils with similar twisted structures but of different heights are presented in Fig. 3*A*. The μFS can simultaneously record quantitative nanomechanical maps (Fig. 3*B*) and topography (24). Unlike the topography image, in which the color contrast relates to height difference, here the color in the stiffness maps presents the hardness; the softer features appear darker. Comparing the topography images and the corresponding stiffness map, the structures and mechanical properties can be correlated. Clearly, although the fibrils have different heights, they share similar stiffness on the crest part (Fig. 3*C*), much softer than background substrate. In addition, both ribbons and twisted fibrils (Fig. 3*D*) can be evaluated (Fig. 3*E*) as well. Clearly, according to color contrast, the twisted fibrils are softer than the flat ribbons. A clear difference is observed in the stiffness of the background substrate and that of the two different kinds of hIAPP$_{20–29}$ structures formed during assembly. The background substrate is lowest, but stiffest; the fibril is highest, but displays the least stiffness; the ribbon is lower than the fibril and higher than the substrate, but it is stiffer than the fibril and softer than the substrate. The measured statistical stiffness distributions of the three species are summarized in Fig. 3*G* (fibrils 2.4 ± 1.0 GPa, ribbons 3.7 ± 0.7 GPa, and substrate 8.3 ± 2.8 GPa). The stiffness of fibrils obtained here shows values similar to those obtained in other studies (40, 41). Additionally, Fig. 3*F* also offers extensive insight into the mechanical variation along the fibrils. The twisted fibrils display anisotropic stiffness along the contour length of the fibril itself. The line profiles cc′ and dd′ show the height profile and the stiffness along the twisted ribbon. It is evident that the crest positions of the twisted fibril are softer than the flat positions of the twisted fibril. The value of Young's modulus on the lower positions of the twisted fibril is close to that measured on flat ribbon. The anisotropic fibril structure indicates the possible vacancy along the fibrillar axis. Hence, we propose that the twisted hIAPP$_{20–29}$ fibrils have a helical, hollow structure instead of a simple twisted structure (11) owing to the multistrand twisting; the simple multistrand twisted fibrils are supposed to be isotropic, including mechanical properties. This agrees very well with the ribbon-like pack model previously proposed (26).

Furthermore, cryotransmission electron microscopy (Cryo-TEM) measurements were carried out to investigate the aggregate structures in bulk. Cryotomography (Movie S1) shows the 3D reconstruction of hIAPP$_{20–29}$ fibrils from tilted 2D images. According to the z-slice view of the tomogram from z = 80 to z = 140 (Fig. S4 and Movie S2), the central space of the fibril

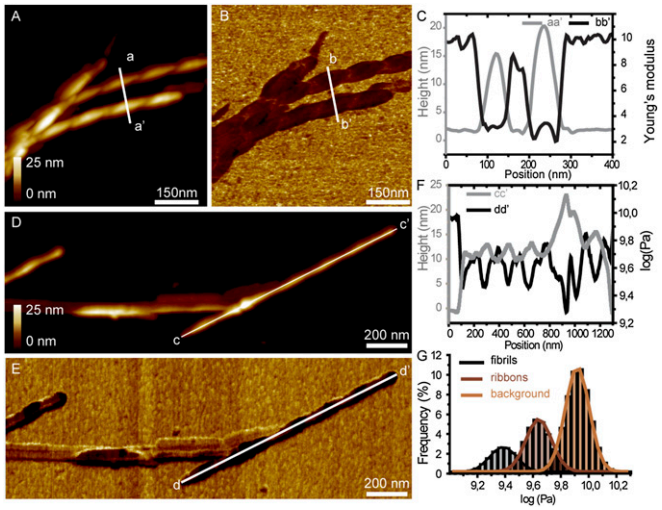

Fig. 3. Quantitative nanomechanical images of hIAPP$_{20–29}$ nanostructures. (*A*) AFM morphology image of two twisting fibrils. (*B*) The corresponding stiffness map of *A*. (C) Line profiles crossing hIAPP$_{20–29}$ fibrils indicated by aa′ in *A* and bb′ in *B*. (*D*) AFM morphology image of hIAPP$_{20–29}$ nanostructures. (*E*) The corresponding stiffness map of *D*. (*F*) Line profiles crossing hIAPP$_{20–29}$ fibrils indicated by cc′ in *D* and dd′ in *E*. (*G*) Stiffness value distributions.

indicates an anisotropic feature because the contrast of the fibril (indicated by blue arrow in Fig. S4) changes according to slice angle. This is considered direct evidence supporting the helical fibril proposal.

Side-Chain Mutations in hIAPP$_{20–29}$ Can Eliminate the Formation of Helical Fibrils. It is well known that the hydrophobic interactions between the side chains of amino acids play an important role in the self-assembly of amyloid proteins (42). Hence, two mutants of hIAPP$_{20–29}$, H-SNNFGAVLSS-NH$_2$ (A$_{26}$G) and H-SNNFGGILSS-NH$_2$ (I$_{27}$V) (Fig. 4*A*), were synthesized to decrease the size of side chains to explore the effect of the morphology and mechanical properties. Previously we have reported that these two mutants only form flat ribbons (35). The same is seen in the present study (Fig. 4 *B* and *D*). Here we extend this work to include the corresponding stiffness maps (Fig. 4 *C* and *E*). These maps result in a value of Young's modulus of 3.7 ± 1.6 GPa for A$_{26}$G and 3.8 ± 1.4 GPa for I$_{27}$V, similar to that of the flat WT hIAPP$_{20–29}$ ribbons (3.7 ± 0.7 GPa). The mutated ribbons have a thickness similar to that of WT hIAPP$_{20–29}$ (Fig. S5); thus, the mutations do not change the mechanical properties of the ribbon. The dominance of the flat ribbons in the mutations is a good indication that the side-chain interaction may be involved in the folding transition.

Molecular-Resolution Model for hIAPP Assembly. The morphology data of hIAPP$_{20–29}$ self-assembly nanostructures provide information on the thickness, periodicity, and twisting angle (summarized in Table 1). These values were used to generate a tentative molecular model using coordinates from the previously determined solid-state NMR structure (21). The model was built using cylindrical coordinates assuming that the subribbon axis is coincident with the fibril axis derived from the solid-state NMR data. Monomers are appended along the subribbon axis using the translation vector found in the NMR structure. The ribbon is built by adding further monomer in a direction orthogonal to the subribbon axis and along the β-strand axis. The ribbon is finalized by increasing the thickness by adding new monomers in a direction orthogonal to the two previous directions.

Fig. 5*A* presents the ribbon-like pack models of the fibrils with various numbers (indicated by II, III, and IV along the cross-section) of ribbon strands with the same periodicity (around 203.8 nm) for the individual strands (although the distances between the individual protofilaments are reduced in the fibrils with higher numbers of strands). Different from the multistranded ribbons (Fig. S6), the proposed models reveal a hollow cross-section in each case, as apparent from a view perpendicular to the fibril cross-section. It is obvious that the more strands the fibril has, the thicker it is (Fig. 5*A Right*). Note that the hollow appearance was not modeled explicitly but was derived as a result of the other morphology parameters listed above and hence validates the derived model. Fig. 5*B* further highlights the subribbon arrangement. In general, each residue in a β-strand arrangement extends the strand by ∼3.2Å, making a single hIAPP$_{20–29}$ peptide ∼3 nm long. According to our AFM data, the width of a single strand is 19.0 ± 1.0 nm, which thus implies that one individual strand seems to contain six to seven peptide molecules. Using a recent solid-state NMR structure of the NFGAIL part of hIAPP$_{20–29}$ amyloid fibrils (21) (extended by MD to include the terminal SN and SS residues in the SNNFGAILSS sequence; Fig. 5*B Upper*), Fig. 5*C* provides tentative structural models of the individual molecules in a β-sheet structure compatible with our AFM data with the structures shown using different viewpoints.

Discussion

Although the hierarchical ribbon-like close-packing scheme was proposed more than 10 y ago for amyloid fibrils (26), few studies have followed the whole self-assembly process quantitatively, especially using short amyloid peptide sequences (15, 36). By means of high-resolution AFM and μFS, we identify the temporal evolution of the polymorphic states of hIAPP$_{20–29}$ and report on their quantitative thickness/height distribution during the initial 5 h (Fig. 1*H*) of the fibrillation process. During the first 2 h of fibrillation, single subribbons are formed through liquid crystalline interactions (43). Later, the short distance attraction force between the single-strand ribbons and oligomers leads to more mature, multistranded ribbons. Finally, some of the flat ribbons begin to twist after the first 2 h. Interestingly, the height distribution of the flat ribbons changes during the end plateau phase of fibrillation (ThT assay in Fig. 1*A*), resulting in stable, flat ribbons once they exceed a threshold height, allowing them to be identified in Figs. 1*G* and 2*A*. We observe examples of ribbons, thicker than 8 nm, surviving and coexisting with helical fibrils. Hence, we propose that when the thickness of the ribbon exceeds a certain threshold (Fig. S7) the ribbon may be energetically stable, and survive (44). Conversely, thinner ribbons have two possible configurations: They can either change to fibrils (Fig. S7) or thicken further to ∼8 nm in height, in which case they remain stable as ribbons and further transition will not occur. This observation differs from the traditional understanding of the relationship between amyloid fibrils and their protofibrils, in which the protofibrils completely turn into fibrils (45). The existence of ribbons

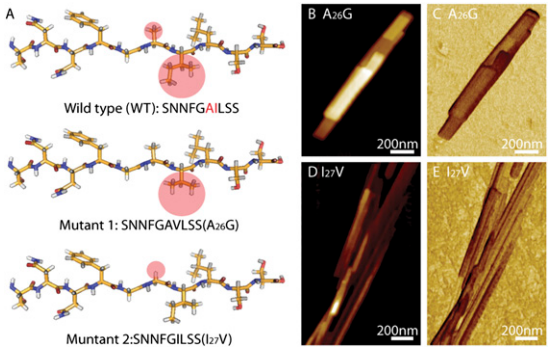

Fig. 4. Mutants of hIAPP$_{20–29}$ and their morphology images and stiffness map. (*A*) The chemical structures of hIAPP$_{20–29}$ and mutants (A$_{26}$G and I$_{27}$V); the light red circles indicate the mutant residues. (*B* and *C*) Topography image and corresponding stiffness map of A$_{26}$G. (*D* and *E*) Topography image and corresponding stiffness map of I$_{27}$V.

Table 1. Statistical morphology data of hIAPP$_{20–29}$ nanostructures with SD

Morphology	Height (nm)	Width (nm)	Twisted angle (°)	Periodicity (nm)
Ribbon	7.4 ± 0.6	19.0 ± 1.0	N.A.	N.A.
Fibril 1	15.5 ± 0.4	39.0 ± 1.5	21.2 ± 0.9	202.3 ± 25.7
Fibril 2	22.9 ± 0.3	59.5 ± 1.2	21.0 ± 1.2	206.2 ± 27.9
Fibril 3	29.7 ± 0.5	81.8 ± 2.1	21.3 ± 1.0	201.3 ± 29.7

N.A., not applicable.

and fibrils and the transition are also captured by Cryo-TEM, shown in Figs. S8 and S9. Furthermore, by fitting the height distribution of ribbons at different incubation times, we calculate the average thickening speed of ribbons, in the initial 5 h, to be 2.4 nm/h. These results reveal a precise determination of the thickening speed of ribbons. Another important finding, which is at variance with previous reports (11), is that independent of how many single-strand ribbons exist within the fibrils, the periodicity remains constant (i.e., the coiling property of each individual ribbon is constant). This puts an upper limit on the number of ribbons that can be incorporated into the fibril and limits the spectrum of fibril subtypes.

Hollow fibril structures have recently been reported for Alzheimer's Aβ$_{40}$ or Aβ$_{42}$ using electron microscopy and solid-state NMR spectroscopy (27, 46, 47). In these fibrils, the full-length peptides fold as hairpins and align with the long axis to form a β sheet, where the hydrophobic effect drives the formation of the hollow core. However, hIAPP$_{20–29}$ is much shorter than Aβ$_{40}$ and Aβ$_{42}$ (Fig. 4*A*) to form hairpin structure. Hence, the hairpin shape is not a suitable structure for the initial building block of hIAPP$_{20–29}$ in our proposed self-assembly scheme. The cylindrical structure is an energetically favorable configuration compared with other amyloid nanostructures. If the multistranded ribbons keep untwisting and growing in width and thickness, the total energy of the system will increase monotonically. To release system energy, the ribbons twist into the helical fibrils, due to the electrostatic repulsion force. However, the free twisting will cost uncompensated elastic/distortion energy, leading to the disintegration of fibrils in the end. During the self-assembly process an attractive force (hydrogen bonds and hydrophobic interactions) most likely opposes electrostatic repulsion to define the final structures of peptide self-assembly (11, 26). This may explain the coexistence of flat ribbons and helical fibrils: The flattening seen in ribbons is compensated by the energy gained from the stacking of strands, which correlates well with the observation that flat ribbons need to exceed a certain height to transform into twisted fibrils (44). Mutations of individual side chains likely shift this balance and destabilize the tubes sufficiently relative to the twisted ribbons to lead to their complete elimination.

In the past, protein fibrils have been classified as high-performance biomaterials and the molecular origin of the material properties of fibrils has been linked to the extensive backbone hydrogen network seen in fibrils (40). The fibrils analyzed in the present work were found to display mechanical stiffness measured in Young's modulus, in the same range as that found for the fibril of insulin of 3.3 ± 0.4 GPa (41). This common feature is due to fibrils' sharing a common cross-β structure with hydrogen-bonded β strands arranged perpendicular to the fibril axis (48, 49). The mechanical stiffness of fibrils could thus be expected to be a characteristic of fibrils that reflects their common structural motif. Indeed, many fibrils of different proteins have been shown to have similar mechanical properties (40). However, the stiffness of the flat regions of the twisted fibrils corresponds to the stiffness seen for the flat ribbons, which supports the hypothesis that the flat ribbons interconvert into twisted fibrils.

In summary, amyloid peptides hIAPP$_{20–29}$ can be expected to follow predefined pathways that direct the spontaneous self-assembly into multiple different nanostructures. The hollow fibrils show distinct characteristic features of hollow twisting, left-handed chirality, and constant periodicity. The quantitative nanomechanical measurements indicate that the twisted conformation represents a decrease in the local stiffness compared with the multistranded ribbon. This is best rationalized as a nanotube with a hollow core. It seems reasonable that the helical hollow structure is the final stage of a fibrillation process, because helical fibrils are more thermodynamically stable (50). Our proposed amyloid self-assembly model provides an unprecedented opportunity to enable spatial localizing of the β sheets along the amyloid fibers, contributing to a new way of understanding the polymorphisms of amyloid peptides.

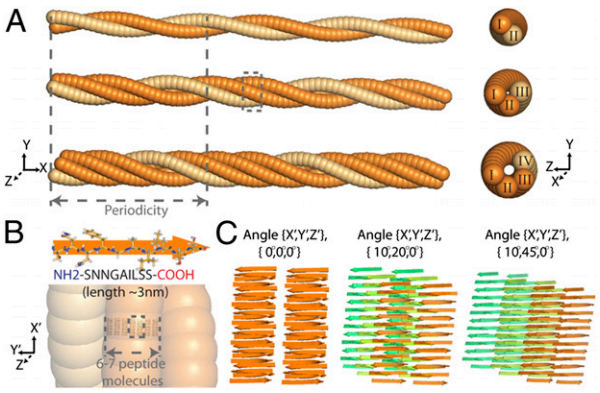

Fig. 5. The reconstruction model of helical fibrils from the multistranded ribbons, based on statistical analysis of AFM data and the previously published solid-state NMR structure (21). (*A*) The helical hollow fibrils with two-, three-, and four-strand subribbons; the right side shows cross-section views indicating the number of subribbons (roman numerals) and the hollow conformation. An axis frame is shown highlighting the fibril and cylinder axis (x). (*B*) The chemical structure of hIAPP $_{20–29}$ (*Upper*) and zoom-in on the model in a view having in the plane of the paper the subribbon axis (x′) and the β-strand axis (y′). The molecular structure is shown as single sheets embedded in the full model. (*C*) Zoom-in on the molecular structure showing the stacked layers from three different viewing angles.

Materials and Methods

Peptide Synthesis. WT hIAPP$_{20–29}$ (H-SNNFGAILSS-NH$_2$) and mutants H-SNNFGGILSS-NH$_2$ (GGIL) and H-SNNFGAVLSS-NH$_2$ (GAVL) were synthesized and purified as described previously (35).

Fibrillation of Peptides and Analogs. WT hIAPP$_{20–29}$ and mutants were dissolved in DMSO to 25 mM and subsequently diluted 1:100 into 50 mM Hepes buffer (pH 7.2) and filtered through a 0.2-μm filter unit. ThT was added to the protein solution to a final concentration of 40 μM and the protein solution was transferred to a 96-well black Costar polystyrene microliter plate, sealed to prevent evaporation, and placed in an Infinite M200 plate reader (Tecan Nordic AB). The plate was incubated at 37 °C, and the ThT fluorescence (excitation 450 nm, emission 482 nm) was measured every 5 min with 3 min of shaking between each reading. During time-lapse analysis of the fibrillation, samples were removed from the plate after 0, 1, 1.5, 2, 5, and 24 h of incubation.

Atomic Force Microscopy. Five microliters of hIAPP$_{20–29}$ solution was deposited onto the freshly cleaved mica surface, air-dried for 5 min, and finally dried with N_2 gas. All of the AFM images were recorded using MultiMode V SPM (Bruker) under ambient conditions. Ultrasharp silicon cantilevers (OMCL-AC160TS-E3; Olympus) were used for time-lapse AFM imaging. Time-lapse AFM imaging was performed in tapping mode at a scan frequency of 1Hz with optimized feedback parameters and 512- × 512-pixel resolution.

Microsecond Force Spectroscopy. The nanomechanical experiments were operated under ambient conditions with a commercial MultiMode V SPM controller (Bruker). A home-built T-shape cantilever (51) was driven at its flexural frequency with a set point of 300–500 mV. The measurement bandwidth was set as 1 kHz by averaging the waveforms over seven consecutive cycles. The resolution of all μFS image is 512 × 512 pixels.

ACKNOWLEDGMENTS. The authors acknowledge financial support from the Centre for DNA Nanotechnology, Center for Insoluble Protein Structures, and from iNANO through the Danish National Research Foundation, the Carlsberg Foundation, and the Villum Foundation. F.S. acknowledges Grant 21261130090 from the National Natural Science Foundation of China.

1. Chiti F, Dobson CM (2006) Protein misfolding, functional amyloid, and human disease. *Annu Rev Biochem* 75(1):333–366.
2. Caughey B, Lansbury PT (2003) Protofibrils, pores, fibrils, and neurodegeneration: Separating the responsible protein aggregates from the innocent bystanders. *Annu Rev Neurosci* 26(1):267–298.
3. Dobson CM (2003) Protein folding and misfolding. *Nature* 426(6968):884–890.
4. Schnabel J (2010) Protein folding: The dark side of proteins. *Nature* 464(7290):828–829.
5. Giehm L, Svergun DI, Otzen DE, Vestergaard B (2011) Low-resolution structure of a vesicle disrupting &α;-synuclein oligomer that accumulates during fibrillation. *Proc Natl Acad Sci USA* 108(8):3246–3251.
6. Cooper GJ, et al. (1987) Purification and characterization of a peptide from amyloid-rich pancreases of type 2 diabetic patients. *Proc Natl Acad Sci USA* 84(23):8628–8632.
7. Nilsson MR (2004) Techniques to study amyloid fibril formation in vitro. *Methods* 34(1):151–160.
8. Petkova AT, et al. (2002) A structural model for Alzheimer's β -amyloid fibrils based on experimental constraints from solid state NMR. *Proc Natl Acad Sci USA* 99(26):16742–16747.
9. Wasmer C, et al. (2008) Amyloid fibrils of the HET-s(218-289) prion form a β solenoid with a triangular hydrophobic core. *Science* 319(5869):1523–1526.
10. Liu P, et al. (2012) Co-assembly of human islet amyloid polypeptide (hIAPP)/insulin. *Chem Commun*, 48:191–193.
11. Adamcik J, et al. (2010) Understanding amyloid aggregation by statistical analysis of atomic force microscopy images. *Nat Nanotechnol* 5(6):423–428.
12. Dong MD, Hovgaard MB, Xu SL, Otzen DE, Besenbacher F (2006) AFM study of glucagon fibrillation via oligomeric structures resulting in interwoven fibrils. *Nanotechnology* 17(16):4003–4009.
13. Yu Y-P, et al. (2012) 2D amyloid aggregation of human islet amyloid polypeptide at the solid-liquid interface. *Soft Matter* 8:1616–1622.
14. Quist A, et al. (2005) Amyloid ion channels: A common structural link for protein-misfolding disease. *Proc Natl Acad Sci USA* 102(30):10427–10432.
15. Adamcik J, Castelletto V, Bolisetty S, Hamley IW, Mezzenga R (2011) Direct observation of time-resolved polymorphic states in the self-assembly of end-capped heptapeptides. *Angew Chem Int Ed Engl* 50(24):5495–5498.
16. Westermark P, et al. (1987) Amyloid fibrils in human insulinoma and islets of Langerhans of the diabetic cat are derived from a neuropeptide-like protein also present in normal islet cells. *Proc Natl Acad Sci USA* 84(11):3881–3885.
17. Janson J, et al. (1996) Spontaneous diabetes mellitus in transgenic mice expressing human islet amyloid polypeptide. *Proc Natl Acad Sci USA* 93(14):7283–7288.
18. Westermark P, Engström U, Johnson KH, Westermark GT, Betsholtz C (1990) Islet amyloid polypeptide: Pinpointing amino acid residues linked to amyloid fibril formation. *Proc Natl Acad Sci USA* 87(13):5036–5040.
19. Tenidis K, et al. (2000) Identification of a penta- and hexapeptide of islet amyloid polypeptide (IAPP) with amyloidogenic and cytotoxic properties. *J Mol Biol* 295(4):1055–1071.
20. Madine J, et al. (2008) Structural insights into the polymorphism of amyloid-like fibrils formed by region 20-29 of amylin revealed by solid-state NMR and X-ray fiber diffraction. *J Am Chem Soc* 130(45):14990–15001.
21. Nielsen JT, et al. (2009) Unique identification of supramolecular structures in amyloid fibrils by solid-state NMR spectroscopy. *Angew Chem Int Ed Engl* 48(12):2118–2121.
22. Tycko R (2011) Solid-state NMR studies of amyloid fibril structure. *Annu Rev Phys Chem* 62(1):279–299.
23. Bertini I, Gonnelli L, Luchinat C, Mao J, Nesi A (2011) A new structural model of Aβ40 fibrils. *J Am Chem Soc* 133(40):16013–16022.
24. Dong MD, Husale S, Sahin O (2009) Determination of protein structural flexibility by microsecond force spectroscopy. *Nat Nanotechnol* 4(8):514–517.
25. Dong M, Sahin O (2011) A nanomechanical interface to rapid single-molecule interactions. *Nat Commun* 2:247.
26. Aggeli A, et al. (2001) Hierarchical self-assembly of chiral rod-like molecules as a model for peptide β -sheet tapes, ribbons, fibrils, and fibers. *Proc Natl Acad Sci USA* 98(21):11857–11862.
27. Paravastu AK, Leapman RD, Yau W-M, Tycko R (2008) Molecular structural basis for polymorphism in Alzheimer's β-amyloid fibrils. *Proc Natl Acad Sci USA* 105(47):18349–18354.
28. Hamley IW (2007) Peptide fibrillization. *Angew Chem Int Ed Engl* 46(43):8128–8147.
29. Cao P, Raleigh DP (2010) Ester to amide switch peptides provide a simple method for preparing monomeric islet amyloid polypeptide under physiologically relevant conditions and facilitate investigations of amyloid formation. *J Am Chem Soc* 132(12):4052–4053.
30. Khemtémourian L, Doménech E, Doux JPF, Koorengevel MC, Killian JA (2011) Low pH acts as inhibitor of membrane damage induced by human islet amyloid polypeptide. *J Am Chem Soc* 133(39):15598–15604.
31. Wolkers WF, van Kilsdonk MG, Hoekstra FA (1998) Dehydration-induced conformational changes of poly-L-lysine as influenced by drying rate and carbohydrates. *Biochim Biophys Acta* 1425(1):127–136.
32. Harper JD, Lieber CM, Lansbury PT, Jr. (1997) Atomic force microscopic imaging of seeded fibril formation and fibril branching by the Alzheimer's disease amyloid-beta protein. *Chem Biol* 4(12):951–959.
33. Goldsbury C, Kistler J, Aebi U, Arvinte T, Cooper GJS (1999) Watching amyloid fibrils grow by time-lapse atomic force microscopy. *J Mol Biol* 285(1):33–39.
34. Harper JD, Lieber CM, Lansbury PT, Jr (1997) Atomic force microscopic imaging of seeded fibril formation and fibril branching by the Alzheimer's disease amyloid-β protein. *Chem Biol* 4(12):951-959.
35. Andreasen M, et al. (2012) Modulation of fibrillation of hIAPP core fragments by chemical modification of the peptide backbone. *Biochim Biophys Acta* 1824(2):274–285.
36. Lara C, Adamcik J, Jordens S, Mezzenga R (2011) General self-assembly mechanism converting hydrolyzed globular proteins into giant multistranded amyloid ribbons. *Biomacromolecules* 12(5):1868–1875.
37. Chothia C (1973) Conformation of twisted β-pleated sheets in proteins. *J Mol Biol* 75(2):295–302.
38. Polyakov P, et al. (2011) Automated force volume image processing for biological samples. *PLoS ONE* 6(4):e18887.
39. Medalsy I, Hensen U, Muller DJ (2011) Imaging and quantifying chemical and physical properties of native proteins at molecular resolution by force-volume AFM. *Angew Chem Int Ed Engl* 50(50):12103–12108.
40. Knowles TP, et al. (2007) Role of intermolecular forces in defining material properties of protein nanofibrils. *Science* 318(5858):1900–1903.
41. Smith JF, Knowles TPJ, Dobson CM, Macphee CE, Welland ME (2006) Characterization of the nanoscale properties of individual amyloid fibrils. *Proc Natl Acad Sci USA* 103(43):15806–15811.
42. Yan L-M, Tatarek-Nossol M, Velkova A, Kazantzis A, Kapurniotu A (2006) Design of a mimic of nonamyloidogenic and bioactive human islet amyloid polypeptide (IAPP) as nanomolar affinity inhibitor of IAPP cytotoxic fibrillogenesis. *Proc Natl Acad Sci USA* 103(7):2046–2051.
43. Bolisetty S, Adamcik J, Mezzenga R (2011) Snapshots of fibrillation and aggregation kinetics in multistranded amyloid β-lactoglobulin fibrils. *Soft Matter* 7(2):493–499.
44. Fishwick CWG, et al. (2003) Structures of helical β-tapes and twisted ribbons:The role of side-chain interactions on twist and bend behavior. *Nano Lett* 3(11):1475–1479.
45. Ionescu-Zanetti C, et al. (1999) Monitoring the assembly of Ig light-chain amyloid fibrils by atomic force microscopy. *Proc Natl Acad Sci USA* 96(23):13175–13179.
46. Miller Y, Ma B, Tsai C-J, Nussinov R (2010) Hollow core of Alzheimer's Abeta42 amyloid observed by cryoEM is relevant at physiological pH. *Proc Natl Acad Sci USA* 107(32):14128–14133.
47. Zhang R, et al. (2009) Interprotofilament interactions between Alzheimer's Abeta1-42 peptides in amyloid fibrils revealed by cryoEM. *Proc Natl Acad Sci USA* 106(12):4653–4658.
48. Eanes ED, Glenner GG (1968) X-ray diffraction studies on amyloid filaments. *J Histochem Cytochem* 16(11):673–677.
49. Serpell LC, Fraser PE, Sunde M (1999) X-ray fiber diffraction of amyloid fibrils. *Methods Enzymol* 309:526–536.
50. Pashuck ET, Stupp SI (2010) Direct observation of morphological transformation from twisted ribbons into helical ribbons. *J Am Chem Soc* 132(26):8819–8821.
51. Sahin O, Magonov S, Su C, Quate CF, Solgaard O (2007) An atomic force microscope tip designed to measure time-varying nanomechanical forces. *Nat Nanotechnol* 2(8):507–514.